water

MDPI

Article

Influence of Different Valve Openings on the Structural Dynamic Characteristics of a Multistage Pump

Guidong Li [1,2,*], Yinling Xia [1], Jieyun Mao [1,2,*], Danhua Zhao [3] and Qi Meng [1]

[1] Research Center of Fluid Machinery Engineering and Technology, Jiangsu University, 301 Xuefu Road, Zhenjiang 212013, China; xyl07141976784508@163.com (Y.X.); mengqi0710@126.com (Q.M.)
[2] Wenling Fluid Machinery Technology Institute of Jiangsu University, Wenling 317525, China
[3] Taizhou Special Equipment Inspection and Testing Research Institute, Wenling 317525, China; auto8787@163.com
* Correspondence: gdli@ujs.edu.cn (G.L.); mjygijon@163.com (J.M.)

Abstract: In order to study the influence of regulating valve openings on the dynamic characteristics of the rotor structure of a multistage pump during the transient startup process, a seven-stage pump was selected as the research object. The transient startup of the pump was jointly simulated using Flowmaster and CFX, and the deformation law of the rotor under different valve openings with time was investigated through Workbench. The results showed that the deformation trends of the impellers at each stage were similar under different valve openings during transient startup, and regulating the valve opening had little significant impact on the stability of the rotor structure. The maximum deformation of the pump shaft occurred at the contact surface between the intermediate impeller and the pump shaft under different valve openings. As the valve opening increased, the maximum deformation of the pump shaft decreased slightly. This study reveals the structural characteristics of the multistage pump during the transient startup process under different valve openings, which is of great importance for improving the safety and reliability of multistage pumps during emergency operations.

Keywords: multistage pump; transient startup; regulating valve openings; transient internal flow field; structural dynamics

Citation: Li, G.; Xia, Y.; Mao, J.; Zhao, D.; Meng, Q. Influence of Different Valve Openings on the Structural Dynamic Characteristics of a Multistage Pump. *Water* **2024**, *16*, 2964. https://doi.org/10.3390/w16202964

Academic Editor: Helena M. Ramos

Received: 22 September 2024
Revised: 10 October 2024
Accepted: 15 October 2024
Published: 17 October 2024

1. Introduction

Multistage pumps are characterized by their compact size, light weight, and high head capabilities, making them widely used in various fields such as high-rise building water supply, agricultural irrigation, fire-fighting pressure boosting, chemical and pharmaceutical industries, HVAC systems (heating, ventilation, and air conditioning systems), etc. Due to their short transient startup time, the transient characteristics of multistage pumps deviate from their steady characteristics. The operational parameters undergo rapid changes, which leads to instantaneous flow and pressure surges. Ensuring smooth pump operation during startup is therefore crucial for the safe and efficient operation of the system. During the rapid startup process, the pipeline system is subjected to the effects of the excitation source, causing the flow state to become extremely complex. Particularly when the impeller rotational speed undergoes rapid changes, different startup and shut-down methods and time can significantly impact the internal flow mechanisms of the pump. In practical operation, variations in valve opening can also lead to rapid changes in the flow velocity, pressure, and flow rate, resulting in an unsteady internal flow field that affects the overall stability of the system [1–3].

Researchers have published some studies on the unsteady phenomena induced by unstable flow, which may affect the flow in the pump during the startup process of the pump [4,5]. Li et al. [6] successfully predicted the transient flow of a centrifugal pump

during the rapid startup process using the dynamic slip region method. The study investigated the relationship between the transient internal flow evolution of the centrifugal pump during the rapid startup process and the corresponding transient flow, head, efficiency, and power. The flow acceleration and transient hydraulic loss or the evolution of the main vortex during the startup process are the main reasons for the transient head coefficient being lower than the quasi-steady-state value. For the low-specific-speed centrifugal pump, the reverse flow at the inlet only affects the dominant performance in the initial stage of the startup. Duplaa et al. [7] investigated the behavior of a centrifugal pump under cavitating and non-cavitating conditions, including steady-state flow and rapid startup. The effect of cavitation on the pump head at constant speed was analyzed, as well as the different types of unsteady behaviors obtained during transients under cavitating conditions. The study showed that low final flow rates usually lead to low cavitation conditions at the end of startup, while increasing the final flow rate leads to more developed cavitation conditions, resulting in a progressive decrease in the pump head. Conversely, low final flow rates can lead to water hammer phenomena associated with a complete and sudden collapse of the steam in the pump and/or inlet pipe. Tanaka et al. [8] conducted experiments and computational fluid dynamics studies on the transient behavior of a rapid startup centrifugal pump. The study pointed out that the dynamic operating point and shaft torque during the pump startup process deviated from the quasi-steady-state change. By comparing with the CFD calculation results, they believed that the reason why the transient characteristics deviated from the quasi-steady-state change was that the formation of the flow field in the pump was delayed relative to the steady-state flow field.

In addition, the unsteady phenomena induced by unstable flow during the startup of the pump also have a certain impact on the stable operation of the system [9,10]. Chalghoum et al. [11] conducted transient calculations of a centrifugal pump with different startup times and different valve openings through numerical simulation, revealing the changes in the transient characteristics of the internal flow and the influence of the valve opening on the pressure fluctuation during the startup process. Li et al. [4] simulated and predicted the fluctuations in pressure and head caused by the sudden opening of a valve. During the valve opening process, the effect of the impeller–volute interaction on pump performance decreases, while the rotation of the vortex plays an increasing role. Experimental results show that during the pump startup process, higher and faster transient responses can be obtained by controlling the assistant valve. It is recommended that the most suitable startup method for the pump valve is T_c (the closed time of the valve) = T_o (the opening time of the pump) − T_v (the opening time of the valve), which can achieve the maximum flow rate and lower maximum pressure. Fu et al. [12] adopted a combined method of numerical simulation and experimentation to investigate the flow behavior and transient characteristics during the startup process of an axial flow pump. The transient impact characteristics caused by the transient startup of the pump are notably evident, with backflow, flow separation, and vortices filling the entire impeller flow passage. During pump startup, the vortex core region gradually increases in size, appearing in large quantities at the leading edges of the blades and within the impeller flow passage at t = 0.6 s, before subsequently decreasing. Zhou et al. [9] conducted numerical simulations of the unsteady startup processes for both single-volute and double-volute centrifugal pumps. They obtained the variation trends of the radial forces acting on the impeller and the volute during startup and analyzed the characteristics of the radial forces and the evolution of the internal flow fields under the two different volute configurations. Chen et al. [13] investigated the internal vortex identification, entropy production, and time-frequency pressure pulsation of a multistage pump under different startup times and flow rate variations. The results showed that a shorter startup time exacerbated the transient effect, with the head increasing rapidly initially and then stabilizing. The vortex structure showed periodic development and dissipation. Entropy production increased with increasing impeller speed, reaching higher peaks at shorter startup times. The blade pass frequency dominated the pressure pulsation, and low-frequency pulsations increased with increasing

speed. However, current research focuses on the unstable flow field phenomena, such as the changes in external characteristics and the evolution of internal flow characteristics during the startup process of the multistage pump. However, the impact of the adjustment of the valve opening during the startup process on the flow characteristics and operational reliability of the multistage pump is still unclear. Therefore, it is necessary to explore the unstable flow phenomenon under different valve opening changes of the multistage pump and consider the dynamic characteristics of the rotor structure under the action of fluid-solid coupling in order to reveal the evolution mechanism of the internal flow characteristics of the multistage pump when adjusting the valve opening, as well as further analyze the influence of flow field changes on the structural deformation and vibration characteristics of the rotor components.

In this study, Flowmaster is integrated with ANSYS CFX to conduct a joint simulation focusing on the transient startup process of a multistage pump. Using the one-way fluid–structure interaction approach, this study focuses on the structural dynamic properties of the multistage pump under different valve openings. The objective is to uncover the effect of valve opening on the mechanism evolution of flow characteristics and the structural deformation of the rotor components, providing some references on enhancing the reliability and operational efficiency of multistage pumps.

2. Numerical Simulation and Experimental Verification

2.1. Computational Model and Meshing

In this study, a seven-stage centrifugal pump equipped with guide vanes serves as the primary subject of analysis. A comprehensive three-dimensional model of the entire flow domain was developed using Pro/Engineer. The hydraulic model is composed of main components such as the impeller, guide vanes, pump casing, and inlet and outlet extensions, as shown in Figure 1. The main design parameters are as follows: design flow rate Q_d = 12 m^3/h, head H_d = 70 m, and rotational speed n_d = 3500 r/min, with more design parameters shown in Table 1.

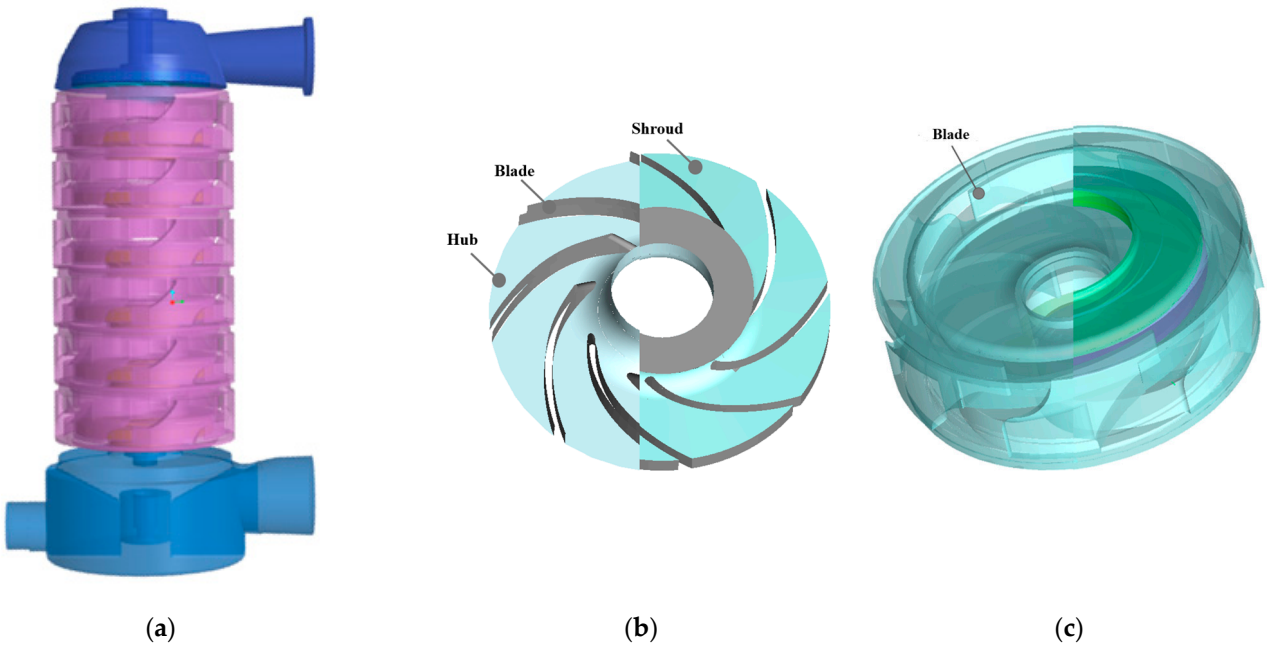

(**a**) (**b**) (**c**)

Figure 1. Three-dimensional model of the multistage pump. (**a**) Hydraulic model of the multistage pump; (**b**) Impeller; (**c**) Guide vane.

Table 1. Main design parameters of the multistage pump.

Design Parameters	Symbol	Value
Design power	P	4 (kW)
Impeller blades number	Zi	8
Impeller inlet diameter	D_1	48.4 (mm)
Impeller outlet diameter	D_2	89 (mm)
Blade outlet width	b_2	6 (mm)
Guide vane outlet diameter	D_0	117 (mm)
Guide vane blades number	Z_g	6
Inlet diameter of suction chamber	D_{in}	51.4 (mm)
Outlet diameter of pressure chamber	D_{out}	50 (mm)

In this study, ANSYS ICEM 2022 software was employed for the mesh generation of the hydraulic components within a multistage pump. Hexahedral structured grids were applied to the impeller region to achieve superior accuracy. Meanwhile, in other computational domains characterized by complex geometries, tetrahedral unstructured grids were adopted due to their flexibility and adaptability. The details of the meshing strategy are shown in Figure 2. Aiming to strike a perfect balance between simulation precision and computational efficiency, a grid independence test was conducted using a single-stage pump as the test subject. The results indicated that a total mesh of approximately 5.8 million for the single-stage pump configuration provided the optimal balance, ensuring both accuracy and efficiency. Finally, a total mesh of approximately 42.2 million for the seven-stage pump was selected for the final computations.

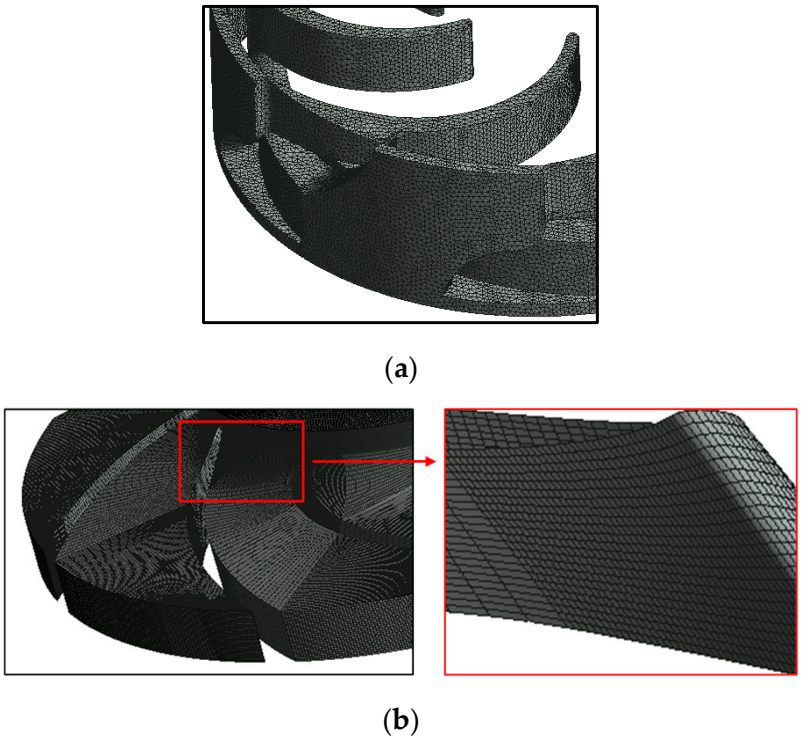

Figure 2. Computational meshes for the impeller and guide vane. (**a**) Guide vane; (**b**) Impeller.

2.2. Boundary Condition Settings

The renormalization group (RNG) *k-ε* turbulence model was selected for the steady-state simulation calculations, adopting ANSYS CFX due to its robustness and accuracy in predicting turbulent flows. The inlet boundary was set as the pressure inlet. The outlet boundary was set as a mass flow outlet to accurately capture the flow dynamics within the pump. The surface roughness of the impeller walls was specified as 50 μm. A convergence

criterion of 10^{-5} was employed to ensure the numerical solution reached a stable and reliable state, thereby enhancing the overall accuracy of the simulation results. In the unsteady simulations, the boundary conditions at the inlet and outlet were maintained to ensure consistency with the steady simulations. In addition, the rotational speed of the impeller, which varies with time during the startup process, was modeled through the integration of user-defined functions. These functions were loaded into the rotating domain within the simulation setup. According to research findings [14–16], it was established that during the pump's startup phase, the rotational speed typically follows an exponential variation with startup time t:

$$n(t) = n_f\left[1 - exp\left(-\frac{t}{T_{na}}\right)\right] \quad (1)$$

where n_f is the stabilized rotational speed after startup and T_{na} is the nominal acceleration time when the speed rises from 0 r/min to 63.2% of 3500 r/min, which equals 0.367 s in this study.

The transient analysis module of the Flowmaster 2020 software is equipped with robust capabilities to simulate the flow state during the actual startup process. Many researchers have validated its accuracy and feasibility through physical model validations [17,18]. In order to analyze variations in the performance parameters of multistage pumps during the startup process, such as flow rate, power, and head, and reveal the changing patterns of their transient characteristics, the relationship between the flow rate and time in the transient startup process was obtained through modeling and simulation using Flowmaster. The operational model diagram for the valve opening startup of a multistage pump is shown in Figure 3.

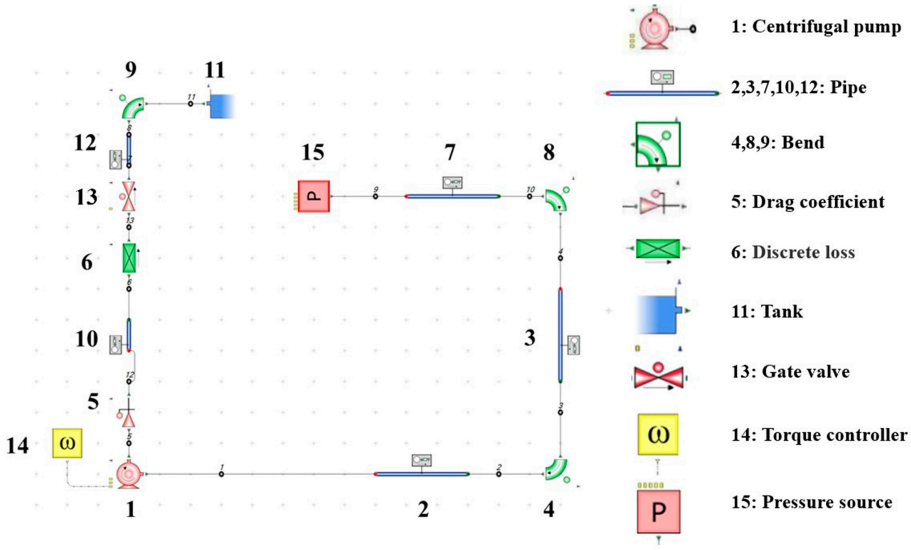

Figure 3. The operational model diagram for the valve opening startup of the multistage pump.

Figure 4 presents the characteristic curves of rotational speed and flow rate versus time for a multistage pump during the startup process, with the outlet valve adjusted to different opening positions. For the *n*-*t* curve, it is evident that within the time interval $t = 0 \sim t_1 = 0 \sim 0.42$ s, the rotational speed rises rapidly. During the interval $t = t_1 \sim t_2 = 0.42 \sim 0.69$ s, the rate of increase in rotational speed decreases, with the value increasing from 2400 r/min to 2950 r/min. Within the interval $t = t_2 \sim t_3 = 0.69 \sim 2.2$ s, the rate of increase in rotational speed further decelerates. After $t_3 = 2.2$ s, the rotational speed gradually approaches a constant value of 3500 r/min. The blue curve in Figure 4 represents the *Q*-*t* variation curve, where $K_V = 0.1 \sim 1.0$ indicates adjusting the outlet valve opening from position 0.1 to the fully open position of 1.0. It is observed that during the initial stage

of startup, the rate of increase in flow rate lags significantly behind the rate of increase in rotational speed. Within the interval t = 0~0.3 s, the flow rate remains relatively stable with minor fluctuations, possibly due to the initially stationary fluid within the pipeline suddenly beginning to accelerate as the pump starts. From t = 0.42 s to t = 3 s, the flow rate enters a rapid increase phase. After the startup is complete at t = 3 s, the rate of increase in flow rate gradually slows down and stabilizes. Additionally, as the valve opening increases, the final stabilized flow rate value correspondingly increases.

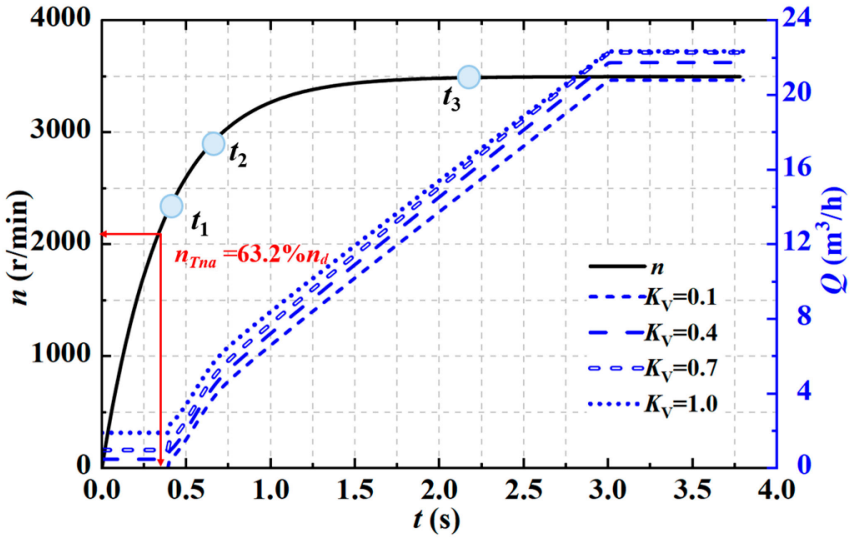

Figure 4. The variation curves of rotation speed and flow rate with time during the startup process under different valve openings (t_1 = 0.42 s, n_1 = 2400 r/min; t_2 = 0.69 s, n_2 = 2950 r/min; t_3 = 2.2 s, n_3 = 3500 r/min).

2.3. Comparative Analysis of Numerical Simulation and Experimental Results

The performance characteristic tests conducted for the multistage pump were performed on a closed-circuit test bench, as shown in Figure 5. The experimental system primarily consisted of a multistage pump, a piping system, valves, an electromagnetic flowmeter, pressure sensors, and a data acquisition system. To avoid the potential for randomness and error inherent in the experimental process, multiple replicates of the flow-head data were collected. The variations in the performance characteristics of the multistage pump are described in dimensionless form in terms of flow and head, as plotted in Figure 6. The definitions for the dimensionless head and dimensionless flow rate are given as follows:

$$\phi = Q/\pi D_2 b_2 u_2 \quad (2)$$

$$\psi = 2gH/u_2^2 \quad (3)$$

where u_2 is the impeller outlet circumferential velocity, m/s; D_2 is the impeller outlet diameter, mm; and b_2 is the impeller outlet width, mm.

Figure 7 presents a comparison of the head between the experimental result and numerical simulations. It is evident that the trends in head variation are consistent. The head error is approximately 4.6% at small flow rates, while it is around 8.6% at large flow rates, which validates the reliability of the numerical simulation calculations.

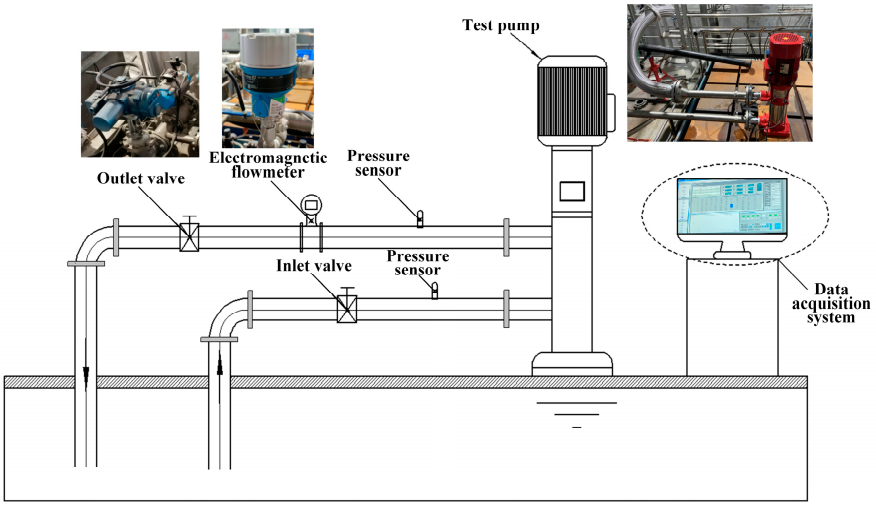

Figure 5. Diagram of the experimental system.

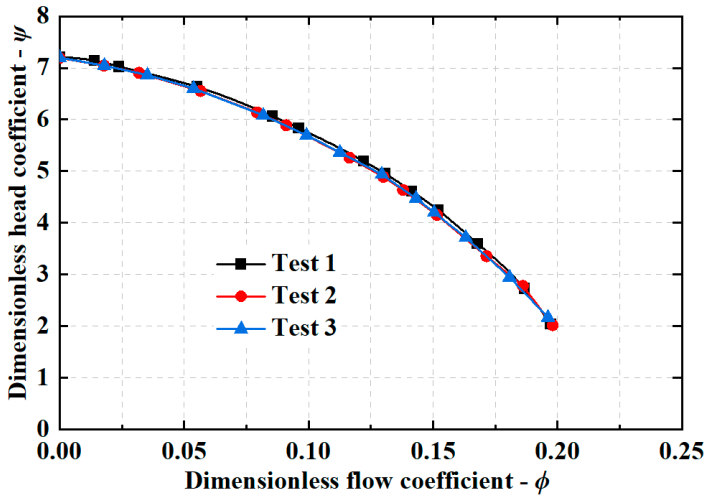

Figure 6. Hydraulic performance characteristic repeated trials.

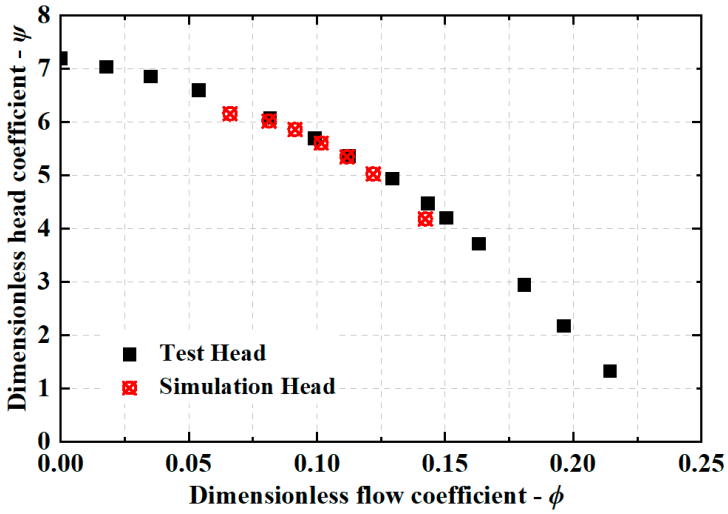

Figure 7. Comparison of head curves between test and numerical simulation results.

3. Results and Analysis

3.1. Analysis of Transient Internal Flow Characteristics

Figure 8 illustrates the distribution of turbulent kinetic energy across the first-stage impeller and the guide vane section of a multistage pump during startup under different valve opening conditions. It can be seen that the variations of turbulent kinetic energy within the guide vane and impeller exhibit a degree of similarity when the valve opening is adjusted. During the initial stages of startup, specifically at n = 1000 r/min (as shown in Figure 4), the turbulent kinetic energy values within the guide vane flow passage are relatively low and exhibit insignificant fluctuations. As the rotational speed progressively increases to n = 2950 r/min, there is an obvious variation in the overall turbulent kinetic energy, and an increase in the values. When the rotational speed reaches the design speed of n = 3500 r/min, the flow within the pump has fully developed, leading to a noticeable reduction in turbulent kinetic energy values compared to in the acceleration phase of rotational speed. It has the advantage of decreasing energy loss and enhancing pump stability. Moreover, under the same rotational speed but with varying valve openings, the flow state within the pump evolves more rapidly as the valve opening increases.

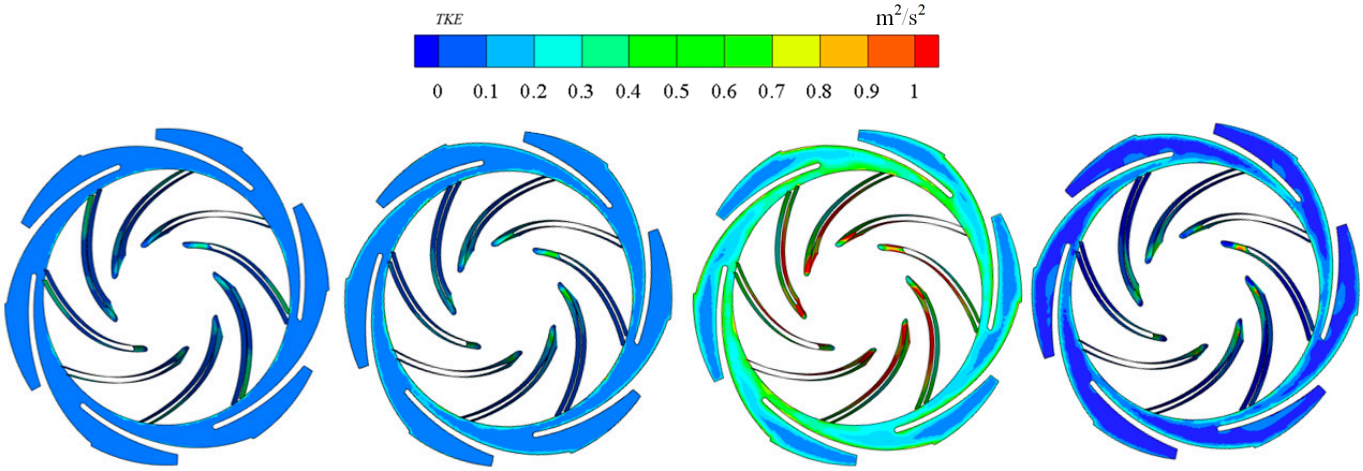

(**a**) K_V = 0.1

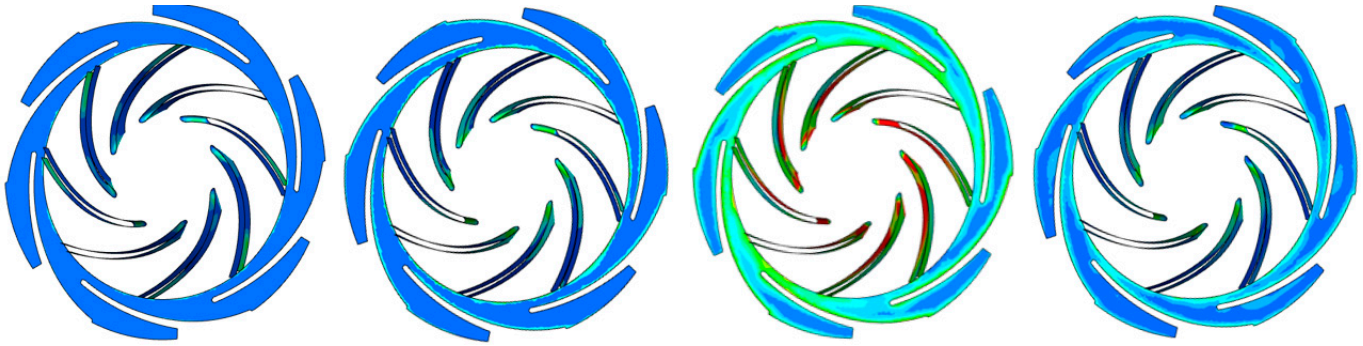

(**b**) K_V = 0.4

Figure 8. *Cont.*

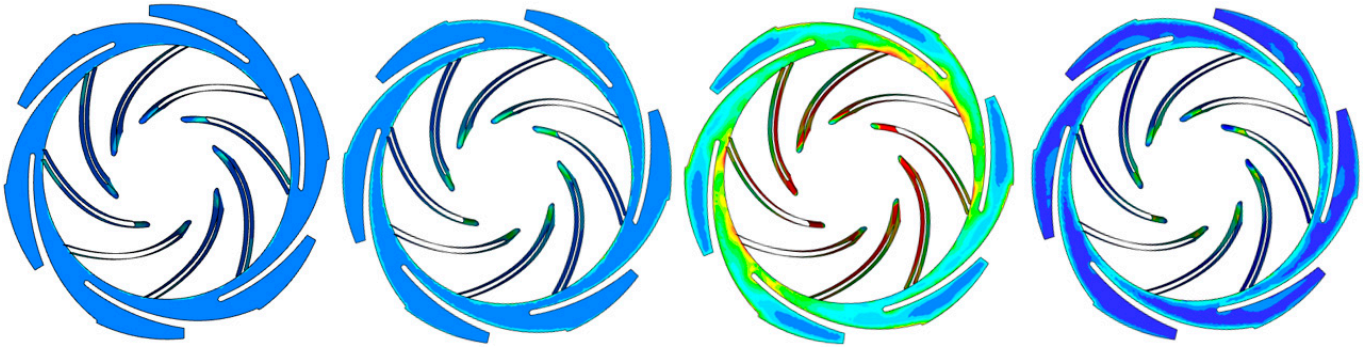

(**c**) $K_V = 0.7$

1000 r/min 2000 r/min 2950 r/min 3500 r/min

Figure 8. Distribution of turbulent kinetic energy changes in guide vanes during the transient startup process.

During the startup process, the fluid is subjected to instantaneous impacts, leading to rapid changes in the flow state and hydraulic characteristics within the hydraulic components. Unfavorable flow states are often accompanied by hydraulic phenomena such as vortices, which can adversely affect the operational stability of the pump. The Ω criterion is a method for identifying vortices, characterized by a normalized threshold. The threshold is normalized between 0 and 1, enabling a clear representation of the strength of vortex cores. Liu et al. [19] decomposed vorticity into rotational and non-rotational components through Equations (4) and (5), where A represents the rotational component and the non-rotational component is denoted as $(\nabla \times V -)$. R characterizes the vortex through the ratio of the rotational component of vorticity to the total vorticity in Equation (6).

$$\omega = \nabla \times V = A + (\nabla \times V - A) \tag{4}$$

$$\begin{aligned} \nabla \times V = & \left(\nabla \times V \cdot \frac{A}{\|A\|}\right) \frac{A}{\|A\|} + \left[\nabla \times V - \left(\nabla \times V \cdot \frac{A}{\|A\|}\right) \frac{A}{\|A\|}\right] = \\ & \sqrt{R} \parallel \nabla \times A \parallel \frac{A}{\|A\|} + \left(\nabla \times V - \sqrt{R} \parallel \nabla \times A \parallel \frac{A}{\|A\|}\right) \end{aligned} \tag{5}$$

$$R = \frac{(\nabla \times V \cdot A)^2}{\parallel \nabla \times V \parallel \parallel A \parallel^2} \tag{6}$$

where ω denotes the total vorticity, A is the vertical vorticity, $\nabla \times V$ denotes the vorticity vector, $\parallel \parallel$ denotes the paradigm operation, and R varies in the range of [0, 1], representing pure deformation when $R = 0$ and pure rotation when $R = 1$.

Based on Equations (4) to (6), $\Omega > 0.5$ can serve as a criterion for vortex identification, meaning that a ratio greater than 0.5 typically indicates the presence of rotation. The threshold value R for the Ω vortex identification method is usually in the range of 0.51 to 0.60. Referring to the recent studies by Zhang [20] and Liu [21,22], $\Omega = 0.52$ is generally chosen as the isosurface to display the vortex structure. Traditional vortex identification methods are reliant on the selection of threshold values. However, there is no concrete value for the threshold R. An incorrect choice of threshold might result in the failure to identify certain vortex structures within the flow field or lead to misjudgment. In contrast, the Ω vortex identification method has the advantage of a clearer physical significance, effectively eliminating the influence of shear layers and accurately capturing the strength of vortices. Therefore, this study will employ the Ω vortex identification method to identify the evolution of the vortex structure within the flow field of a multistage pump.

Figure 9 presents the variations in vortex structures within the first-stage impeller by using the Ω vortex identification method under different valve openings. As illustrated in Figure 9a, the sudden startup of the pump at t_1 results in an instantaneous pressure impact on the static fluid by the moving components, leading to an unstable flow state. Due to the

abrupt change in flow velocity as the fluid passes from the impeller inlet to the passages, many vortices can be captured near the hub. Moreover, energy exchange occurs between the fluid near the inlet hub and the main flow (the fluid passes from the impeller inlet to the passages), leading to a higher concentration of vortices near the leading edge of the blades (as shown in the red rectangular region). At t_2, the vortices initially attached to the blade leading edge continue to develop and expand in size and display a chaotic distribution, forming a multitude of low-energy filamentous vortices at the impeller outlet. Until t_3, the vortices attached to the blade leading edge break up, and the filamentous vortices adhering to the impeller outlet break into sporadic and patchy structures.

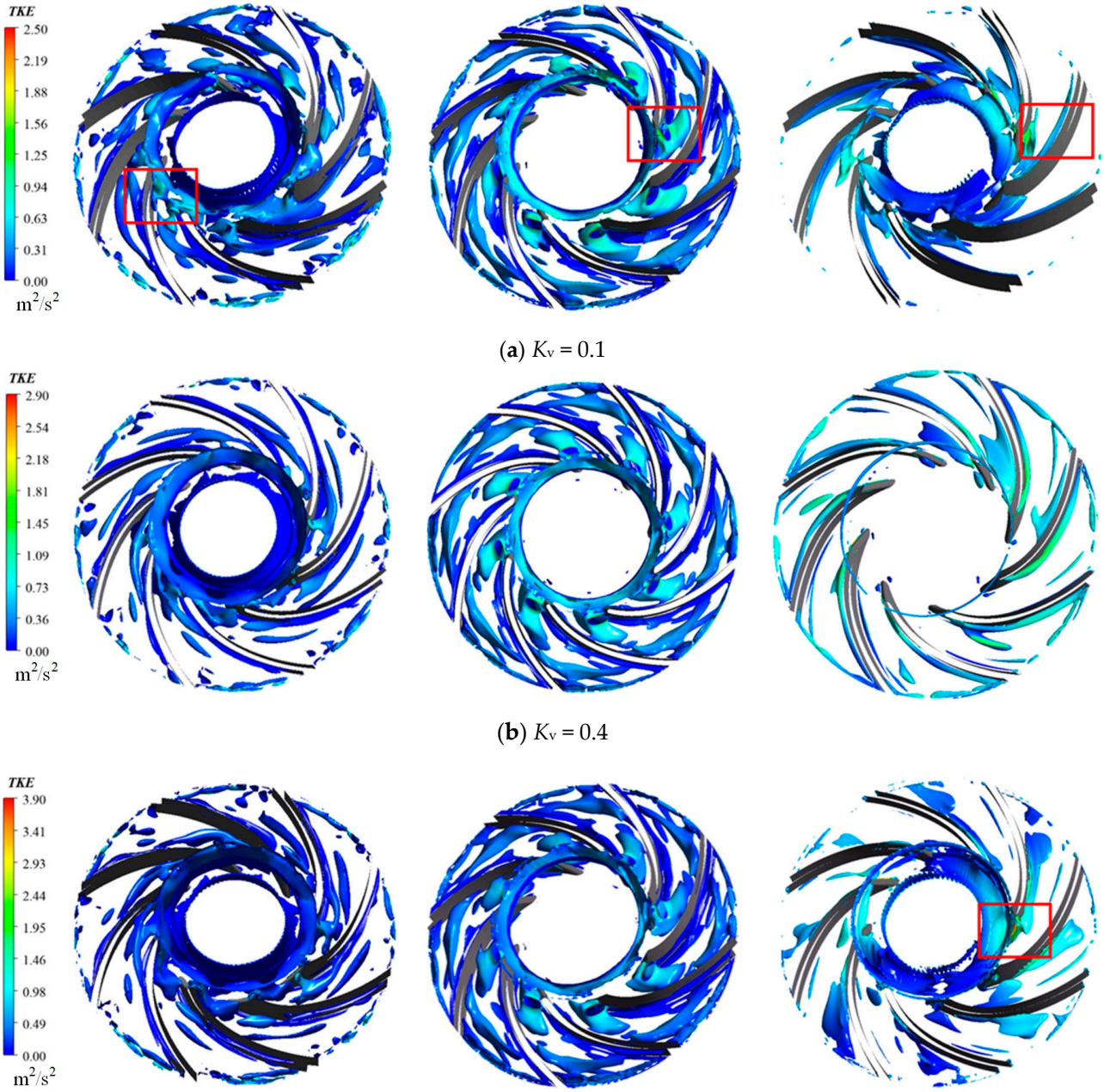

Figure 9. The evolution process of the vortex volume within the first-stage impeller at K_v = 0.1, 0.4, and 0.7.

As the valve opening increases to K_V = 0.4 in Figure 9b, it is evident that the unstable structures within the impeller passage have notably diminished in comparison to K_V = 0.1. In Figure 9c, a substantial dissipation of vortices concentrated near the impeller blades is observed, with most appearing in elongated shapes predominantly situated on the pressure side of the blades. To summarize, during the initial startup and under smaller valve openings, vortices of varying energy levels continuously collide within the impeller passage. As the startup time progresses and the valve opening increases, the number of vortices decreases significantly, and the internal flow field of the pump gradually transitions towards a state of stability.

3.2. Analysis of Structural Dynamic Characteristics

3.2.1. Calculation Model and Boundary Condition Settings

The meshing operation for the rotor structure and pump shaft was performed using the Mesh module in ANSYS Workbench, as illustrated in Figure 10a,b. The mesh size of the impeller area was set to 3 mm, the mesh size of the blade surface was set to 2 mm, and the mesh size of the pump shaft was set to 5 mm. The total number of mesh elements was approximately 10^7. Based on the principle of one-way fluid–structure interactions, structural deformation and stress were analyzed. The transient startup results of the multistage pump were loaded into the structural field for an iterative solution. The selected flow rates were consistent with those during the transient simulation, namely $Q = 0.42\ m^3/h$ at t_1, $Q = 4.2\ m^3/h$ at t_2, and $Q = 15.5\ m^3/h$ at t_3. Centrifugal force, fluid forces, and gravitational loads were applied to the structural domain. In this study, the centrifugal force is mainly applied to the solid domain by applying the rotational speed to the rotating parts. The magnitude of the rotational speed and the application method are consistent with the settings in Section 2.2. The internal flow field force was the transient simulation results applied in the form of pressure loads to the impeller hub, shroud, and fluid–solid coupling interface. The gravitational loads were applied to the rotor system in the form of gravity acceleration. The constraints for the impeller and pump shaft are shown in Figure 10c, while the primary material property parameters are described in Table 2.

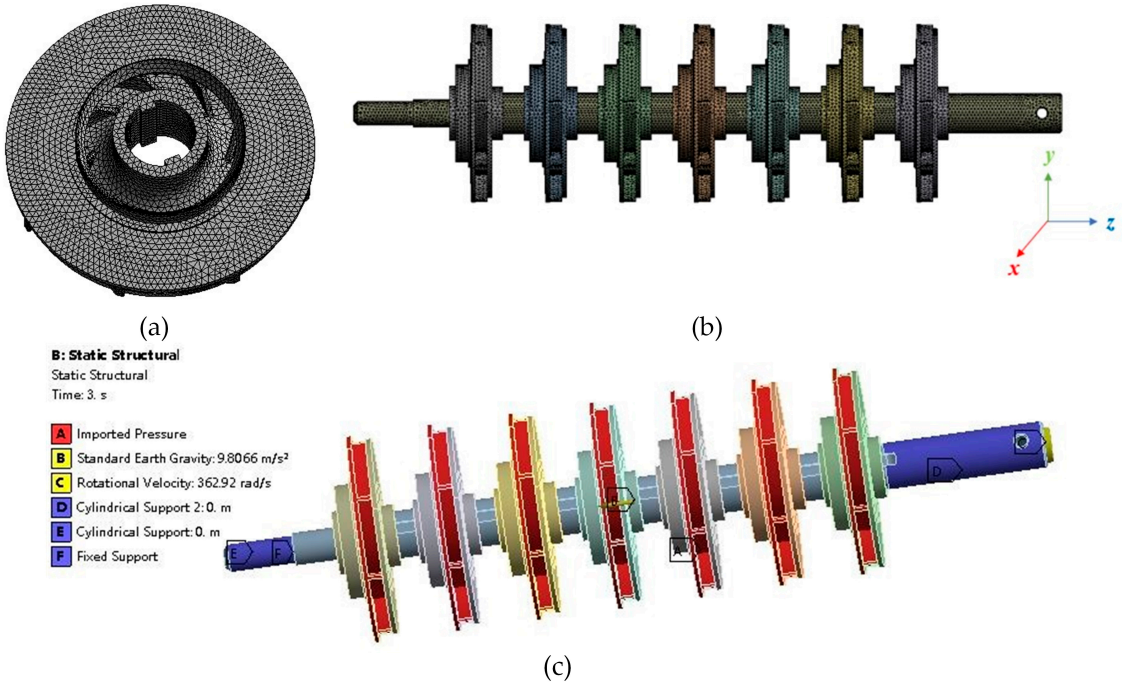

Figure 10. Mesh and constraint settings. (**a**) Impeller; (**b**) Impeller and pump shaft; (**c**) Rotor structure load constraint settings.

Table 2. The physical property parameters of the pump material.

Model	Material	Density [kg/m^3]	Young's Modulus [GPa]	Poisson Ratio	Tensile/Compressive Strength [MPa]
Pump shaft	S304	7930	193	0.3	205
Impeller	PPO	1080	0.3	0.38	63.4

3.2.2. Modal Analysis of Rotor Structure

Figures 11 and 12, respectively, present the variations in the modal shapes of the rotor structure under conditions without prestress (idle condition, no load) and with prestress (steady condition, Q = 12 m^3/h). It can be seen from Figure 11 that the primary manifestation of the first six modal shapes of the rotor is torsional vibration, which all stretch along the y-direction without significant bending. The maximum deformation for 1~2nd-order modals and 4~5th-order modals predominantly occurs at the middle-stage impeller, specifically near the outer edge of the impeller exit. The location of the maximum bending amplitude for the third-order modal is at the outlet of the first-stage impeller. The location of the maximum bending amplitude for the sixth-order modal is at the outlet of the final-stage impeller.

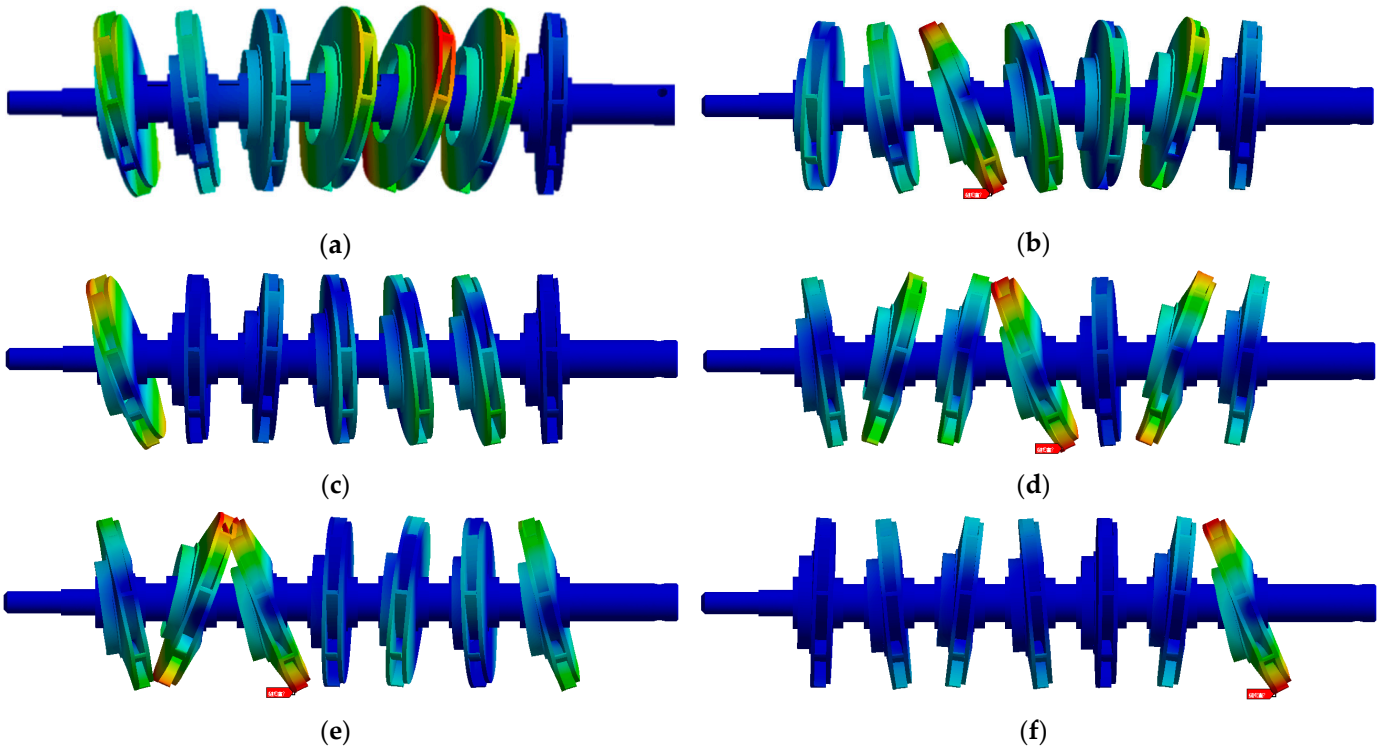

Figure 11. The change of rotor vibration mode without prestress. (**a**) First-order modal; (**b**) Second-order modal; (**c**) Third-order modal; (**d**) Fourth-order modal; (**e**) Fifth-order modal; (**f**) Sixth-order modal.

In contrast to the idle condition, it can be seen from Figure 12 that the rotor components are not only subjected to the effects of rotational centrifugal force but also influenced by the pressure differential within the internal fluid field. The first-order and second-order modals are predominantly characterized by torsional vibrations, with the impeller deformation manifesting as stretching in the y-direction. The third-order modal is characterized by oscillation in the x-direction, a behavior that is similarly exhibited in the fourth-order modal. The fifth-order and sixth-order modals are primarily torsional vibrations, with the impeller deformation presenting as stretching in the x-direction. In general, the rotational

centrifugal force and pressure differential within the fluid field have an obvious effect on the natural frequencies of the third-order to sixth-order modals, while exerting a relatively minor influence on the structural natural frequencies of the first-order and second-order modals. After the imposition of constraints, limiting the structural degrees of freedom has an effect on the modal analysis results. However, according to Table 3, it is observed that the calculated values post-constraint application exhibit a minimal discrepancy when compared to the figures obtained under conditions without prestress. In conclusion, these findings prove that the effects of rotational centrifugal force and forces exerted by the fluid field have a negligible impact on the outcomes of modal analysis.

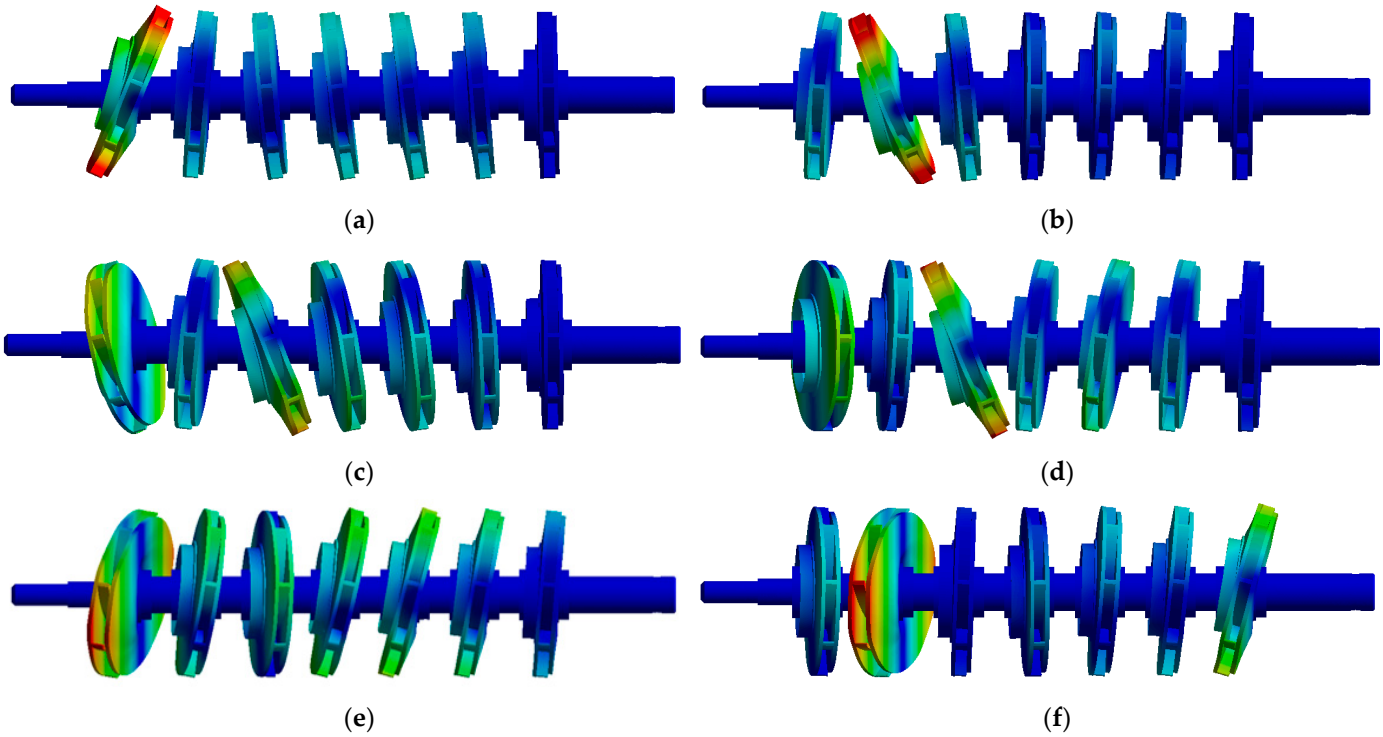

Figure 12. The change of rotor vibration mode with prestress. (**a**) First-order modal; (**b**) Second-order modal; (**c**) Third-order modal; (**d**) Fourth-order modal; (**e**) Fifth-order modal; (**f**) Sixth-order modal.

Table 3. The change of natural frequency and vibration mode of rotor components with and without prestress.

Order	Natural Frequency Without Prestress/Hz	Amplitude Without Prestress/mm	Natural Frequency with Prestress/Hz	Amplitude with Prestress/mm
1	59.9	2.865	75	2.9554
2	64.5	2.851	76.5	2.9537
3	173.99	3.827	176.4	4.3807
4	255.42	6.528	283.61	4.9535
5	379.5	6.646	394.6	6.542
6	564.25	7.002	578.6	7.123

3.2.3. Distribution of Impeller Deformation Under Different Valve Openings

To analyze the impact of the valve opening on impeller deformation in a multistage pump during the transient startup process, the transient flow field calculation results under different valve openings at various startup moments were loaded into the fluid–structure interaction module of ANSYS Workbench. Given the many stages in multistage pumps, the analysis was confined to the impeller deformation at the first, second, fifth, and seventh stages. Figure 13 illustrates the variation of the maximum impeller deformation over

time during the transient startup process. As the number of pump stages increases, each stage impeller transfers energy to the fluid, enabling it to achieve higher pressures and velocities. Correspondingly, the stress on the rotor structure arises with the increase in pressure. This stress contains both radial stress, which is perpendicular to the rotor axis, and axial stress, which is aligned with the rotor axis. Radial stress is primarily a result of the fluid pressure exerted on the impeller blades, whereas axial stress arises due to friction and pressure differentials as the fluid traverses the flow channels within the impeller. These stresses undergo continuous fluctuations during the impeller rotational cycle. If the stresses are larger than the material's tolerance limit, it will lead to impeller deformation and even fractures.

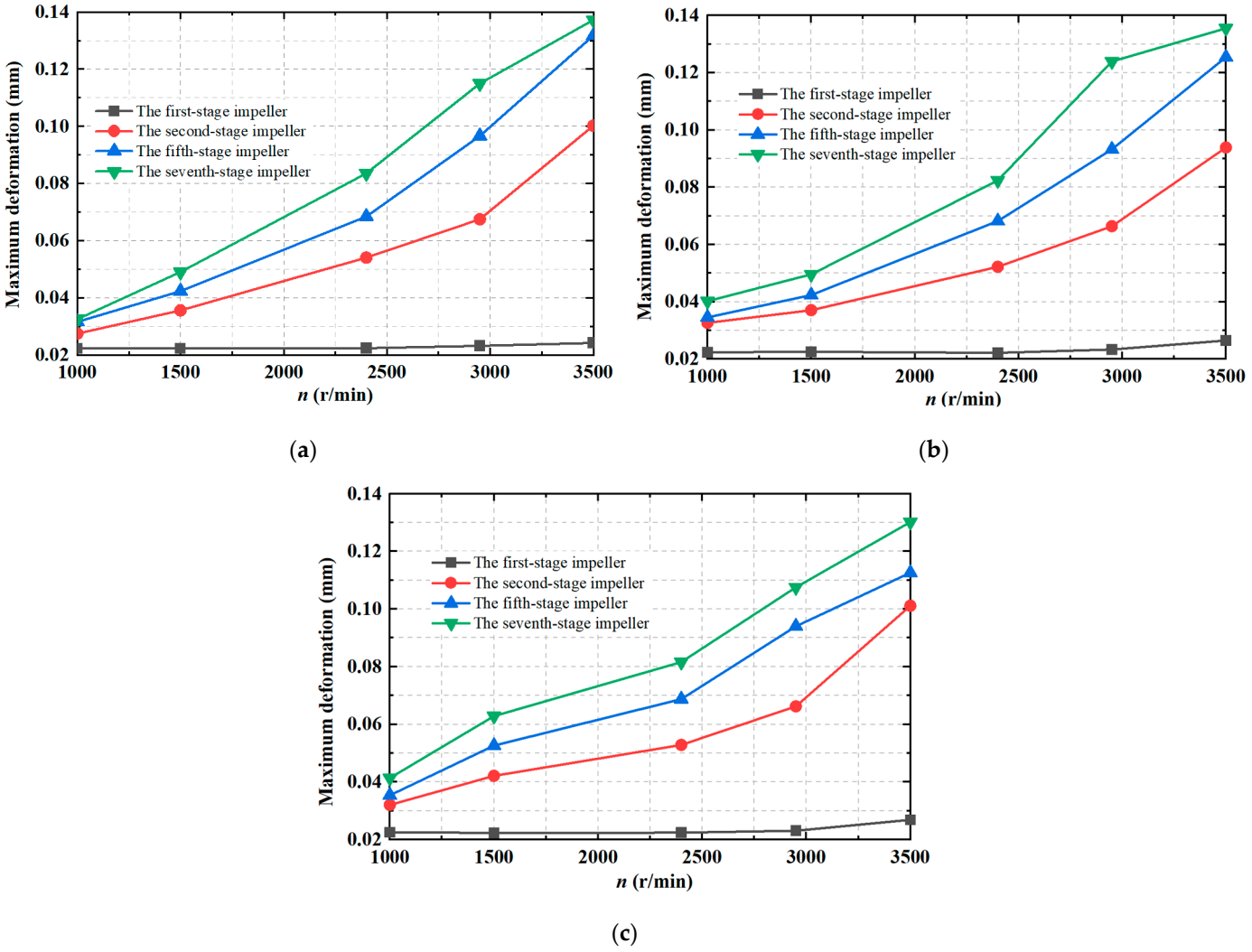

Figure 13. Distribution of maximum impeller deformation during the transient startup process. (**a**) K_V = 0.1; (**b**) K_V = 0.4; (**c**) K_V = 0.7.

It can also be observed that the deformation of the first-stage impeller almost does not change with the increase in rotational speed at K_V = 0.1. At K_V = 0.4 and K_V = 0.7, the deformation of the first-stage impeller begins to undergo a slight change as the rotational speed exceeds 3000 r/min. This phenomenon can potentially be attributed to the fluid within the pump, which has yet to establish a stable flow state in the initial stages of startup. Consequently, the impeller is subjected to relatively smaller inertial and centrifugal forces, resulting in less variations in its deformation.

From the second-stage impeller onwards, with the increase in impeller rotational speed and startup time, the deformation of each impeller stage exhibits an obvious increasing trend. The underlying reasons for this phenomenon can be explained as follows: as the rotational speed increases, the combined influence of the medium pressure, centrifugal force, and frictional forces acting on the impeller intensifies. This will change the force distribution, and then the impeller deformation. Moreover, the fluid–structure interaction between the impeller and fluid can significantly impact the stress distribution across the impeller, thereby contributing to the impeller deformation. Additionally, the presence of unsteady flow may induce instability in the radial forces acting on the impeller, further contributing to variations in the deformation. At K_V = 0.1 and 0.4, the rate of increase in the deformation of the second-stage impeller and the fifth-stage impeller increases with the increment in rotational speed. However, for the seventh-stage impeller, it is characterized by an initial increase followed by a subsequent decrease (particularly at K_V = 0.4). This behavior can potentially be attributed to the fact that during the initial phases of pump startup, the seventh-stage impeller experiences an increase in both centrifugal force and pressure, resulting in a larger deformation. However, as the rotational speed continues to ascend, the operational condition of the seventh-stage impeller approaches its design operating state. At this juncture, the impeller deformation stabilizes and the rate of increase in deformation begins to decrease.

Figure 14 illustrates the deformation distribution of the final-stage impeller at K_V = 0.1, 0.4, and 0.7 (Figure 14a–c at t_1, Figure 14d–f at t_2 and Figure 14g–i at t_3). It can be seen that the maximum impeller deformation exists near the impeller exit for three valve openings. For the same valve opening at different startup times, the maximum impeller deformation markedly increases in comparison to the initial stages of startup as the rotational speed increases to the design value. Under steady operating conditions, the pressure load exerts a predominant influence on the deformation distribution of the impeller. However, during the transient startup process, characterized by rapid changes in the flow state, the variations in flow rate and pressure load have a relatively minor impact on flow pressure distribution, with a maximum of merely 0.13 mm. At t_1, the deformation distribution of the final-stage impeller under different valve openings exhibits a consistent pattern. The maximum deformation of the impeller increases radially as the distance from the impeller hub increases, with the deformation at the front cover plate essentially displaying a central symmetry. At t_2, the maximum deformation of the impeller increases by approximately 0.02 mm. At t_3, when the rotational speed accelerates to 3500 r/min, the deformation distribution becomes uneven. As the valve opening increases, the maximum impeller deformation decreases from 0.137 mm at K_V = 0.1 to 0.130 mm at K_V = 0.7. Generally, the deformation patterns and trends of the final-stage impeller during transient startup are similar across different valve opening openings.

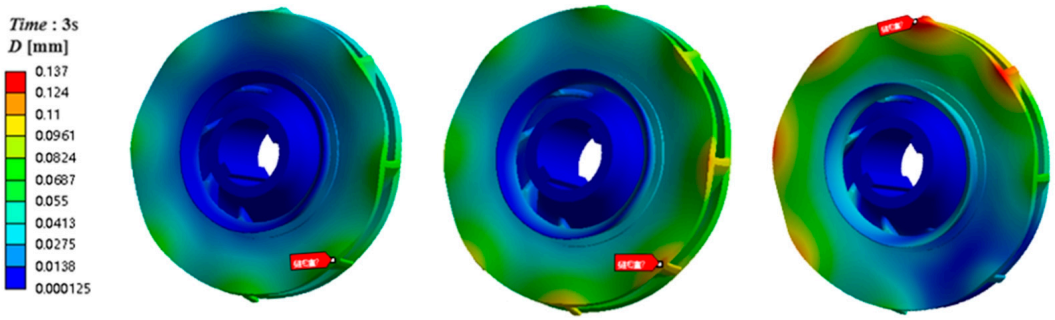

(a) Kv=0.1 (b) Kv=0.4 (c) Kv=0.7

Figure 14. *Cont.*

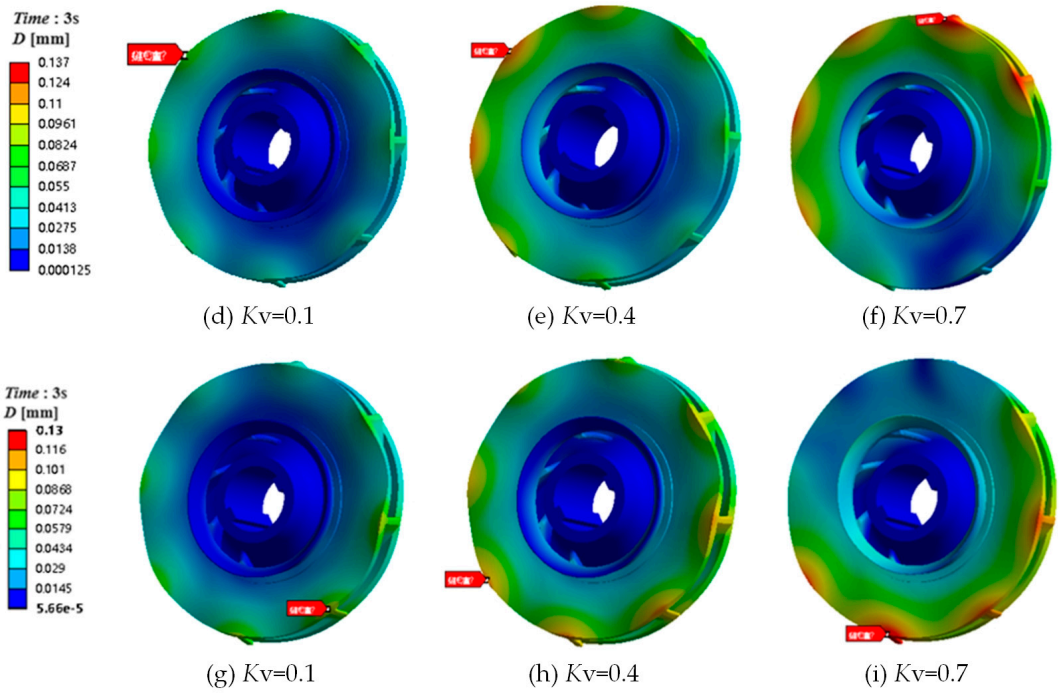

Figure 14. Distribution of deformation of the final stage impeller during the transient startup process ((**a**–**c**) at t_1; (**d**–**f**) at t_2; (**g**–**i**) at t_3).

3.2.4. Distribution of Pump Shaft Deformation Under Different Valve Openings

During the operational cycle of a multistage pump, the interaction between the flow and the impellers is a complex and dynamic phenomenon. The rotation of the impeller induces an acceleration and deceleration effect on the flow. As the water flows through each impeller stage, this cycle of changes in pressure and velocity is repeated, resulting in a periodic pressure fluctuation. While such fluctuations are to some extent normal, excessively intense fluctuations or those that exceed the design threshold can damage the stable operation of the pump. For instance, significant variations in pressure can impose additional stresses on the internal rotor components of the pump, potentially accelerating wear or causing damage. Moreover, these pressure fluctuations can induce vibrations within the pump, which not only reduce the pump efficiency but can also affect the mounting base and surrounding equipment [23]. The radial force F_x in the x-direction and the radial force F_y in the y-direction obtained in transient startup calculations were applied to the cylindrical contact surfaces between the impellers and the pump shaft, respectively. In addition, a time-varying rotational speed was imposed on the pump shaft, consistent with the transient startup rotational speed change in Formula (1).

Figure 15 presents the curves depicting the variation of the transient radial force F acting on the impellers with time under different valve openings during the startup process. Given the multitude of impeller stages, the distribution of radial forces on the rotor system is uneven and lacks a clear principle. Before $t < 2.0$ s, the magnitude of the radial force acting on the rotor system under different valve openings fluctuates significantly. This is because, as the pump begins to operate, the rotation of the impellers generates centrifugal forces, which in turn exert radial forces on the pump shaft. These forces change with the flow of the fluid, particularly as the valve opening varies, leading to significant alterations in the fluid flow state and consequently impacting the forces acting on the pump shaft. In the initial stages of startup, as the valve gradually opens, the transition from a static to a flowing state of the fluid causes a sharp change in the pressure and velocity within the pump, affecting the stability of the pump shaft. As the valve opening increases, the flow rate through the impellers rises, resulting in an increase in the radial force acting on the pump shaft (as in the case of K_V = 0.7). However, this increase is not linear but

rather exhibits a complex dynamic response. In some cases, as the flow rate increases, the maximum deformation of the pump shaft may decrease slightly (as observed at K_V = 0.1). This phenomenon can be attributed to the combined effects of fluid inertia and viscosity. On the one hand, the inertia of the fluid results in a substantial centrifugal force when the impellers are rotating; on the other hand, the viscosity of the fluid exerts a damping effect on the pump shaft, aiding in the reduction of vibrations. These two effects are in competition, ultimately dictating the deformation of the pump shaft.

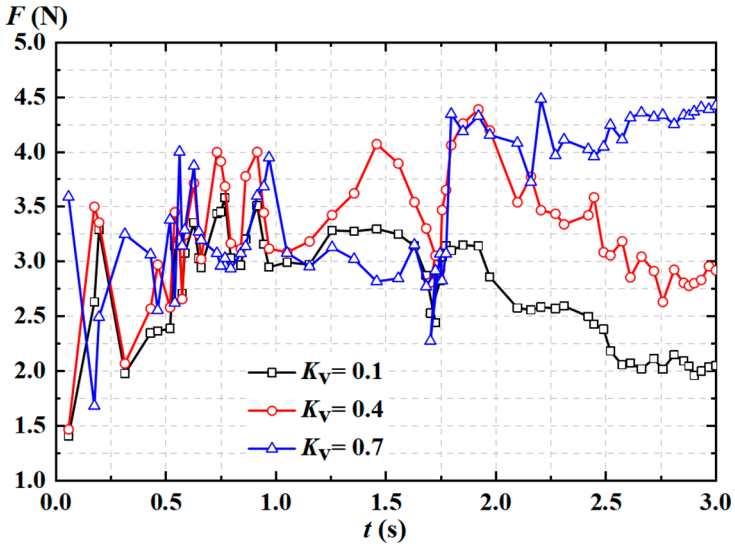

Figure 15. Time-domain plot of transient radial force under different valve openings.

It can also be observed that as the startup time increases (as t > 2.2 s, the rotational speed reaches a stable value), the fluctuation trend of the radial force amplitude becomes more moderate compared to the initial startup phase. This is because, as the rotational speed continues to increase, the fluid in the flow field gradually adapts to the new flow conditions. The turbulence intensity decreases and the flow tends to become more uniform, reducing the flow's instability. Consequently, the fluctuations in the amplitude of the radial force caused by flow instability also decrease correspondingly. Once the rotational speed reaches a stable value, the fluid enters a relatively stable state. The turbulence intensity decreases further, and the flow reaches a more uniform state. The fluctuations in the amplitude of the radial force become smoother, demonstrating a more stable operating condition. In addition, as the start-up time increases, the larger the valve opening, the greater the radial force on the impeller. This may be because as the valve opening increases, the pump flow rate also increases, which will cause the momentum change of the fluid in the impeller to increase, thereby generating a greater force. The liquid pressure between the impeller and the volute will also increase due to the increase in flow, which will generate a greater radial force on the impeller.

The radial force on the impeller monitored in the transient startup calculation was loaded onto the cylindrical contact surface between the impeller and the pump shaft. In addition, a time-varying rotational speed was applied to the pump shaft. The constraint setting of the pump shaft was the same as the rotor structure constraint setting in the previous section.

Figure 16 illustrates the deformation distribution of the pump shaft at the end of the startup process at t = 3.0 s under different valve openings. The deformation of the pump shaft increases gradually from both ends towards the center, reaching a maximum at the contact surface near the middle-stage impeller and the pump shaft. This phenomenon could be attributed to the bending stresses generated by each impeller stage on the shaft. As the number of stages increases, these stresses accumulate along the shaft. It leads to stress concentration near the middle-stage impeller, thus causing the maximum deformation.

Furthermore, as the valve opening increases, increasing the flow rate results in a slight reduction in the maximum deformation.

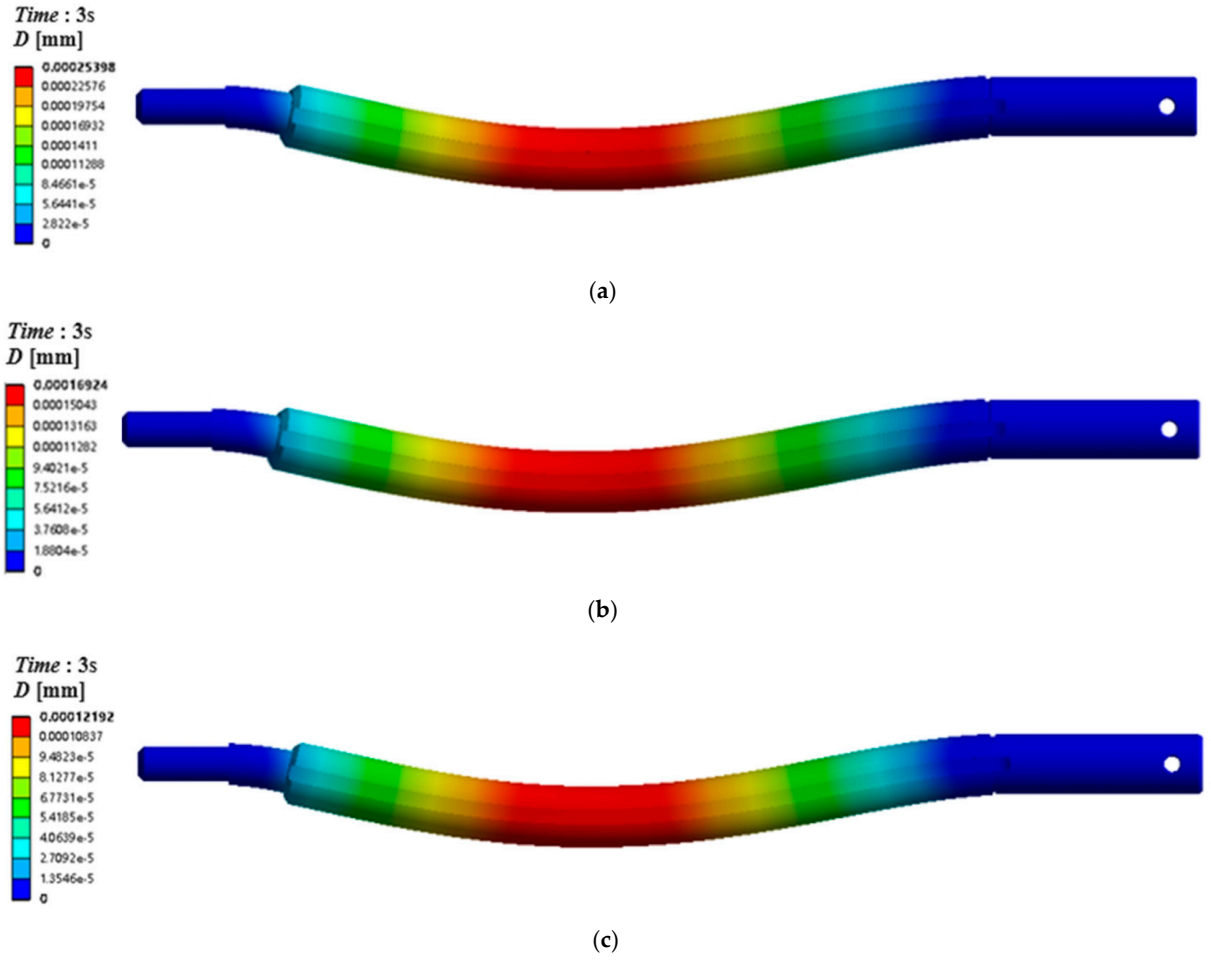

Figure 16. Deformation distribution of the pump shaft under different valve openings at t = 3.0 s. (**a**) K_V = 0.1; (**b**) K_V = 0.4; (**c**) K_V = 0.7.

4. Conclusions

The transient startup process of a seven-stage pump under different valve openings was jointly simulated by using Flowmaster and CFX. The deformation law of the rotor structure with time was investigated through Workbench. The following conclusions were obtained:

(1) During the initial stage of startup, the rate of increase in flow rate lags significantly behind the rate of increase in rotational speed. Within the interval t = 0~0.3 s, the flow rate remains relatively stable with minor fluctuations. From t = 0.42 s to t = 3 s, the flow rate enters a rapid increase phase. After the startup is complete at t = 3 s, the rate of increase in flow rate gradually slows down and essentially stabilizes. Additionally, as the valve opening increases, the final stabilized flow rate value correspondingly increases.

(2) During the initial startup and under smaller valve openings, vortices of varying energy levels continuously collide within the impeller passage. As the startup time progresses and the valve opening increases, the number of vortices decreases significantly, and the internal flow field of the pump gradually transitions towards a state of stability.

(3) The deformation trends of the impellers at each stage are similar under different valve openings during the transient startup process, and regulating the valve opening had little significant impact on the stability of the rotor structure.

(4) Before $t < 2.0$ s, the magnitude of the radial force acting on the rotor system under different valve openings fluctuates significantly. After that the fluctuations become smoother, demonstrating a more stable operating condition. The deformation of the pump shaft increases gradually from both ends towards the center, reaching a maximum at the contact surface near the middle-stage impeller and the pump shaft. Furthermore, as the valve opening increases, the increasing flow rate results in a slight reduction in the maximum deformation.

Author Contributions: Conceptualization, G.L.; Methodology, G.L. and J.M.; Software, Y.X. and Q.M.; Formal analysis, J.M.; Data curation, Y.X.; Writing—original draft, Y.X.; Writing—review & editing, G.L., J.M. and Q.M.; Visualization, D.Z.; Supervision, G.L., J.M. and D.Z.; Funding acquisition, G.L. All authors have read and agreed to the published version of the manuscript.

Funding: This work was supported by the Natural Science Foundation of Jiangsu Province (Grant No. BK20210761), the Special Supported Project of China Postdoctoral Science Foundation (Grant No. 2021TQ0130), the Self-supported Project of Wenling Fluid Machinery Technology Institute of Jiangsu University (Grant No. 01012), and the Taizhou City Social Development Science and Technology Plan Project (Grant No. 23sfb07).

Data Availability Statement: The data that have been used are confidential.

Conflicts of Interest: The authors declare that the research was conducted in the absence of any commercial or financial relationships that could be construed as a potential conflict of interest.

Nomenclature

Symbol	Physical meaning	Symbol	Physical meaning
A	vertical vorticity	T_c	closed time of the valve
D_1	impeller inlet diameter	T_{na}	nominal acceleration time
D_2	impeller outlet diameter	T_o	opening time of the pump
D_{in}	inlet diameter of suction chamber	T_v	opening time of the valve
D_{out}	outlet diameter of pressure chamber	Zi	impeller blades number
D_0	guide vane outlet diameter	b_2	blade outlet width
F	radial force	n	rotational speed
F_x	radial force in the x-direction	n_d	stabilized rotational speed
F_y	radial force in the y-direction	t	startup time
H	Head	u_2	impeller outlet circumferential velocity
H_d	design head	ϕ	dimensionless head
K_V	outlet valve opening	ψ	dimensionless flow rate
P	design power	Ω	strength of vortex cores
Q	flow rate	$\nabla \times V$	vorticity vector
Q_d	design flow rate	$\| \|$	paradigm operation
R	ratio of the rotational component of vorticity to the total vorticity		

References

1. Qin, H.; Ni, H.; Jin, J. Differential evolutionary modeling and starting-up cavitation characteristics analysis for multistage centrifugal pump. In Proceedings of the 2018 IEEE 4th Information Technology and Mechatronics Engineering Conference (ITOEC), Chongqing, China, 14–16 December 2018; IEEE: New York, NY, USA, 2018; pp. 412–416.
2. Long, Y.; Lin, B.; Fang, J.; Zhu, R.S.; Fu, Q. Research on the transient hydraulic characteristics of multistage centrifugal pump during start-up process. *Front. Energy Res.* **2020**, *8*, 00076. [CrossRef]
3. Cui, B.; Zhang, Y.; Huang, Y.; Zhu, Z. Analysis of unsteady flow and fluid exciting forces of multistage centrifugal pump based on actual size. *Proc. Inst. Mech. Eng. Part A J. Power Energy* **2022**, *236*, 21–32. [CrossRef]
4. Li, Q.; Ma, X.; Wu, P.; Yang, S.; Huang, B.; Wu, D. Study on the transient characteristics of the centrifugal pump during the startup period with assisted valve. *Processes* **2020**, *8*, 1241. [CrossRef]
5. Zheng, X.; Wang, W.; Zhang, P.; Pu, Y.; Zhao, Y. Internal flow characteristics of centrifugal pumps under different startup combination schemes. *Water* **2024**, *16*, 1087. [CrossRef]

6. Li, Z.F.; Wu, D.Z.; Wang, L.Q.; Huang, B. Numerical simulation of the transient flow in a centrifugal pump during starting period. *ASME J. Fluids Eng.* **2010**, *132*, 81102. [CrossRef]
7. Duplaa, S.; Coutier-Delgosha, O.; Dazin, A.; Roussette, O.; Bois, G.; Caignaert, G. Experimental study of a cavitating centrifugal pump during fast startups. *ASME J. Fluids Eng.* **2010**, *132*, 021301. [CrossRef]
8. Tanaka, T.; Takatsu, N. Transient characteristics of a centrifugal pump at rapid startup. *J. Phys. Conf. Ser.* **2019**, *240*, 052016.
9. Zhou, R.; Yang, J.; Liu, H.L.; Dong, L. Effect of volute geometry on radial force characteristics of centrifugal pump during startup. *J. Appl. Fluid Mech.* **2021**, *15*, 25–36.
10. Zhang, Y.L.; Ji, Y.Y.; Zhao, Y.J. Deep analysis of the transient behavior of centrifugal pumps during startup and shutdown. *Meas. Control.* **2022**, *55*, 155–163. [CrossRef]
11. Chalghoum, I.; Elaoud, S.; Akrout, M.; Taieb, E.H. Transient behavior of a centrifugal pump during starting period. *Appl. Acoust.* **2016**, *109*, 82–89. [CrossRef]
12. Fu, S.F.; Zheng, Y.; Kan, K.; Chen, H.X.; Han, X.X.; Liang, X.X.; Liu, H.W.; Tian, X.Q. Numerical simulation and experimental study of transient characteristics in an axial flow pump during start-up. *Renew. Energy* **2020**, *146*, 1879–1887. [CrossRef]
13. Chen, C.; Xu, H.; Deng, F.; Wu, K.; Zhang, Z.; Si, Q. Study on the transient flow characteristics of multistage centrifugal pumps during the startup process before system operation. *Water* **2024**, *16*, 1876. [CrossRef]
14. Tsukamoto, H.; Ohashi, H. Transient characteristics of a centrifugal pump during starting period. *Fluids Eng.* **1982**, *104*, 6–13. [CrossRef]
15. Zhang, Y. Transient Internal and External Characteristics During the Start-Up Process of Centrifugal Pumps. Ph.D. Thesis, Zhejiang University, Hangzhou, China, 2013.
16. Li, W.; Lu, D.; Ma, L.; Ji, L.; Wu, P. Experimental study on pressure vibration characteristics of mixed-flow pump during start-up. *Trans. CSAE* **2021**, *37*, 44–50.
17. Li, Y.; Su, H.; Wang, Y.; Jiang, W.; Zhu, Q. Dynamic characteristic analysis of centrifugal pump impeller based on fluid-solid coupling. *Mar. Sci. Eng.* **2022**, *10*, 880. [CrossRef]
18. Zhang, X.; Jiang, Y.; Tang, F.; Song, X.; Liu, Y.; Yang, F.; Shi, L. Investigation on start-up characteristics of large axial flow pump systems considering the influence of auxiliary safety facilities. *Machines* **2023**, *11*, 182. [CrossRef]
19. Liu, C.; Wang, Y.; Yang, Y.; Duan, Z. New omega vortex identification method. *Sci. China Phys. Mech. Astron.* **2016**, *59*, 1–9. [CrossRef]
20. Zhang, Y.N.; Liu, K.H.; Li, J.W.; Xian, H.Z.; Du, X.Z. Analysis of the vortices in the inner flow of reversible pump turbine with the new omega vortex identification method. *Hydrodyn* **2018**, *30*, 463–469. [CrossRef]
21. Liu, C.; Gao, Y.; Tian, S.; Dong, X. Rortex-A new vortex vector definition and vorticity tensor and vector decompositions. *Phys. Fluids* **2018**, *30*, 1–12. [CrossRef]
22. Liu, C.; Gao, Y.; Dong, X.; Liu, C.; Gao, Y.S.; Dong, X.R.; Wang, Y.Q.; Liu, J.M.; Zhang, Y.N.; Cai, X.S.; et al. Third generation of vortex identification methods: Omega and Liutex/Rortex based systems. *Hydrodyn* **2019**, *31*, 205–223. [CrossRef]
23. Jin, F.; Yao, Z.; Li, D.; Xiao, R.; Wang, F.; He, C. Experimental investigation of transient characteristics of a double suction centrifugal pump system during starting period. *Energies* **2019**, *12*, 4135. [CrossRef]